

More than just a wrinkle: A wave-like pattern in U_g vs. L_z from Gaia Data

Jennifer K. S. Friske,^{1*} Ralph Schönrich,²

¹*Ludwig-Maximilians-Universität, Fakultät für Physik, Schellingstr. 4, 80799 München, Germany*

²*University of Oxford, Rudolf Peierls Centre for Theoretical Physics, Clarendon Laboratories, OX1 3PU Oxford, UK*

Accepted XXX. Received YYY; in original form ZZZ

ABSTRACT

We present a newly found wave-like pattern in mean Galactocentric radial velocity \overline{U}_g vs. guiding centre radius R_g or angular momentum L_z of stars in the RV subsample of Gaia DR2. The short-wave pattern has a wavelength of order 1.2 kpc in R_g or 285 kpc km s^{−1} in L_z . The pattern shows only weak changes with Galactocentric radius R and little change in strength in particular with the vertical energy E_z of the stars or respectively the distance to the Galactic plane $|z|$. The pattern is to first order symmetric around the plane, i.e. has no significant odd terms in z . There is weak phase shift with the pattern moving towards slightly lower L_z (i.e. trailing) with $|z|$ and E_z . However, we observe a highly significant phase shift in Galactic azimuth ϕ , which is different for different peaks. The peak around $L_z \sim 2100$ kpc km s^{−1} shows weak/uncertain change and shifts by of order $dL_z/d\phi \sim (97 \pm 32)$ kpc km s^{−1}/rad, while the rest of the pattern shows a clearly detectable shift of (200 ± 22) kpc km s^{−1}/rad. If we consider all peaks to belong to the same pattern, this would suggest a wavenumber $m = 4$. We further find that the wave-like pattern in U_g appears to be related to the \overline{W} vs. L_z pattern detected in Gaia DR1. A comparison of the $\overline{U}_g - L_z$ wave pattern with changes of \overline{U}_g vs. R , which have been previously discussed, suggests that the latter can be understood as just the $\overline{U}_g - L_z$ pattern washed out by blurring (i.e. orbital excursions around their guiding-centre) of disc stars.

Key words: stars: kinematics and dynamics – Galaxy: disc – Galaxy: kinematics and dynamics – Galaxy: solar neighbourhood – Galaxy: structure

1 INTRODUCTION

From its first data release the Gaia satellite mission (Gaia Collaboration et al. 2016a) has been providing a stunning, unprecedented view on disc structure. In fact, we are only very slowly getting to grips with new features in phase space that were not fully anticipated in theoretical models. Given the great technological advance compared to its predecessor Hipparcos (Perryman et al. 1997), we can expect that Gaia’s data will reveal many surprising diagnostics of the disc structure and kinematics that are hidden in plain sight. In this paper, we will discuss a newly found dependence of the mean radial velocity \overline{U}_g on angular momentum L_z , which exhibits a strong wave-like pattern.

One example of beautiful surprises by Gaia has been the discovery of vertical substructure in the motion of disc stars. While its predecessor Hipparcos had just deliv-

ered very tentative evidence for the Galactic warp (Dehnen 1998), molecular gas observations and star counts of bright stars (e.g. Drimmel et al. 2000; Drimmel & Spergel 2001; Reylé, C. et al. 2009) have shown that the Sun is quite close to the line of nodes of a large-scale outer disc warp. We should thus expect stars with large angular momenta to have a positive mean vertical velocity \overline{W} relative to the disc. Instead of just confirming the tentative evidence of the Galactic warp in Hipparcos (Schönrich & Dehnen 2018; Poggio et al. 2018), already Gaia DR1 provided more than a quantification of the warp signal. It revealed the presence of a wave-like pattern with an amplitude of ~ 1 km s^{−1} of \overline{W} vs. L_z with a scale-length of order 500 kpc km s^{−1} or respectively ~ 2 kpc in guiding centre radius R_g (Schönrich & Dehnen 2018). This wave (confirmed later by Seabroke et al. 2018, on Gaia DR2) is likely connected to the much larger waves in the outer disc (Xu et al. 2015; Bergemann et al. 2018): the local amplitude should be a lot smaller due to the much larger local surface density compared to the out-

* E-mail: J.Friske@physik.lmu.de

skirts of the disc. The most likely culprits are also known: the previous impact of the Sagittarius dwarf galaxy and its then a lot more massive dark matter halo, causing a wake in the halo (Weinberg 1995) and then the corrugated warp/wave pattern in the Galactic disc (D’Onghia et al. 2016; Laporte et al. 2018).

Related to this vertical wave-structure, Gaia DR2 directly brought the discovery of the phase-space spiral (Antoja et al. 2018) – a prominent spiral shape in the W - z plane (altitude z above or below the disc plane), which is particular visible if one colours each bin by its mean (galactocentric) azimuthal or radial velocity, \overline{V}_g or \overline{U}_g . The spiral can again be readily explained with an impact and thus resulting vertical impulse on the disc about 300 Myr ago (Binney & Schönrich 2018), although other explanations, e.g. with bar buckling (Khoperskov et al. 2018) have been proposed.

Here, we will show that there is a very clear wave-like pattern present in \overline{U}_g vs. L_z throughout the entire extent (spanning a diameter of more than 4 kpc) probed by the Gaia RV dataset. This dataset adds line-of-sight velocities to the Gaia astrometry and thus provides full 6D phase space information for ~ 7 million objects. In section 3, we describe the data used for our evaluation and how the catalogue used was derived from the Gaia sample. In the following section 4, we present the pattern and investigate its behaviour at different positions in the sample data range. We try to quantify the azimuthal phase shift in subsection 4.2 by fitting a suitable function to our data and give an estimate for the involved wavenumbers. Section 4.3 then investigates correspondences between the $\overline{U}_g - L_z$ pattern and the waves in \overline{W} vs. L_z , as well as the trends in \overline{U}_g vs. galactocentric radius R . Finally, we summarising our findings in 5.

2 COORDINATE FRAME AND DEFINITIONS

We use a standard right-handed coordinate system (U, V, W) for the velocities, where U is the component of motion towards the Galactic Centre, V in the direction of Galactic rotation, and W quantifies the motion upwards, perpendicular to the plane. We distinguish between Galactocentric velocity components (U_g, V_g, W) which are measured in the local Cartesian coordinate system of the star in the rest frame of the Galactic Centre and heliocentric velocity components (U_h, V_h, W_h), which are measured in the Cartesian coordinate system and relative to the motion of the Sun. In other notation systems, U_g would equal $-v_R$ and V_g would equal v_ϕ . Slightly inconsistent in sign and with the handedness of the coordinate system, we define $L_z = RV_g$, positive in the direction of disc rotation. We set the solar Galactocentric radius $R_0 = 8.27$ kpc, the total azimuthal velocity of the Sun $V_{g,\odot}$, and the Local Standard of Rest velocity vector of the Sun $(U_\odot, V_\odot, W_\odot) = (11.1, 12.24, 7.25) \text{ km s}^{-1}$. These values have been taken from Schönrich (2012) and Schönrich et al. (2010) in accordance with Gillessen et al. (2009) and McMillan (2017). The values thus imply a local circular speed $V_c = 238 \text{ km s}^{-1}$, and a solar value $L_{z\odot} = 2067 \text{ kpc km s}^{-1}$. For each star, we make use of Galactocentric cylindrical coordinates, where $R = \sqrt{x^2 + y^2}$ denotes the in-plane Galactocentric radius, and (x, y, z) are the coordinates in the heliocentric Cartesian frame with the Galactic

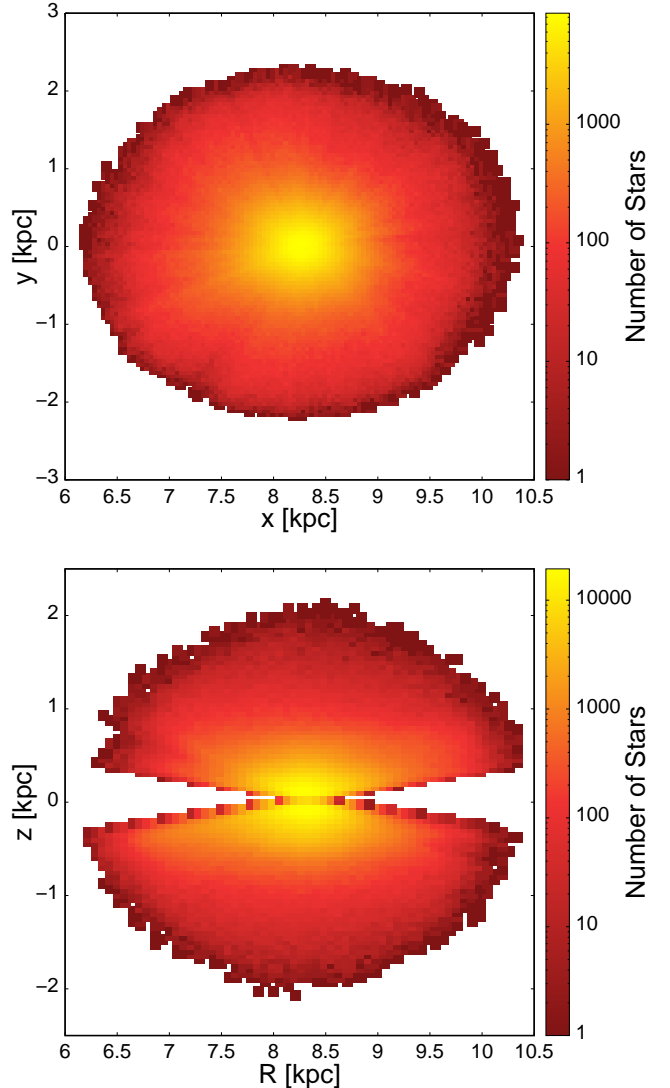


Figure 1. Geometry of the Gaia Sample we used after introducing the various quality cuts explained in section 3

Centre (GC) at $R = x = y = z = 0$, x in the radial direction outwards, y in the azimuthal direction, and z perpendicular to the Galactic plane. We denote Galactic longitude and latitude with (l, b) . An important quantity in our analysis is the azimuth of a star, i.e. the in-plane angle between the connection lines Sun–GC and GC–star. The azimuth is taken positive in the direction of rotation with $\phi = 0$ at the solar position.

3 DATA

In this study we make use of the Gaia RV sample (Cropper et al. 2018; Gaia Collaboration et al. 2018b), which has been published as a part of Gaia DR2 (Gaia Collaboration et al. 2018a). Descriptions of the Gaia spacecraft and of its on-board spectrograph can be found in Gaia Collaboration et al. (2016b) and Sartoretti et al. (2018). To derive the 6D phase space information, we employ the astrometric information from Gaia DR2, which provides

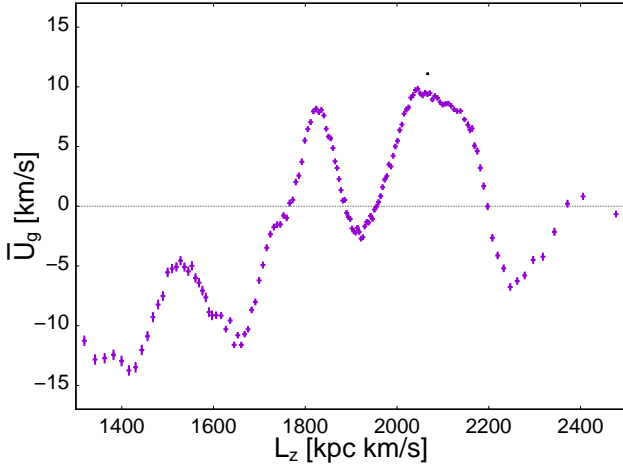


Figure 2. Mean radial velocity component \bar{U}_g of all stars in the sample, when binned by angular momentum L_z . For each data point, 10000 stars (20000 stars for L_z between 1600 km s^{-1} and 2150 km s^{-1}) were taken from the sample sorted in L_z . The error bars depict the Poisson noise in each bin, i.e. σ_{U_g}/\sqrt{N} , where N is the number of stars in each bin and σ_{U_g} its measured dispersion in U_g .

proper motions and parallax measurements (Arenou et al. (2018) and Lindegren et al. (2018)). To provide distances for the sample, we use the distance expectation values from Schönrich et al. (2019), which were derived with the method of Schönrich & Aumer (2017). Using the expectation values for the distance has the advantage that the expectation values of velocity components should be unbiased. The distances have been extensively tested and calibrated the Gaia parallax offset $\delta p = (0.054 \pm 0.06)$ mas (Gaia parallaxes are too small), using the method of Schönrich et al. (2012). The implied offset is substantially (a factor 2) larger than estimated from the Gaia quasar sample in Lindegren et al. (2018). However, the quasar sample is a lot fainter, has a different colour distribution, and has generally zero parallax, factors that advise against a direct extrapolation to the Gaia RV sample. Further, the offset we use is in agreement with tests on particular sources in Stassun & Torres (2018) and Zinn et al. (2018). We employ the quality cuts suggested in section 8 of Schönrich et al. (2019). We furthermore require a parallax quality ratio $p/\sigma_p > 10$ and an additional cut on Galactic latitude of $b > 10$. The resulting distribution of stellar loca can be found in Fig. 1.

4 A NEW WAVE PATTERN IN GAIA DR2

4.1 The pattern of radial motion vs. angular momentum

We can now turn to the topic of this paper: a wave-like structure in the radial velocity component. Fig. 2 shows the mean U_g velocity component in bins of angular momentum. To generate this plot, we ordered the sample in the angular momentum $L_z = RV_g$ of each star. For the well-populated region with L_z between 1600 km s^{-1} and 2150 km s^{-1} we then sliced the sample into bins of 20000 stars each, while we use bins of 10000 stars outside the core region in L_z . All data

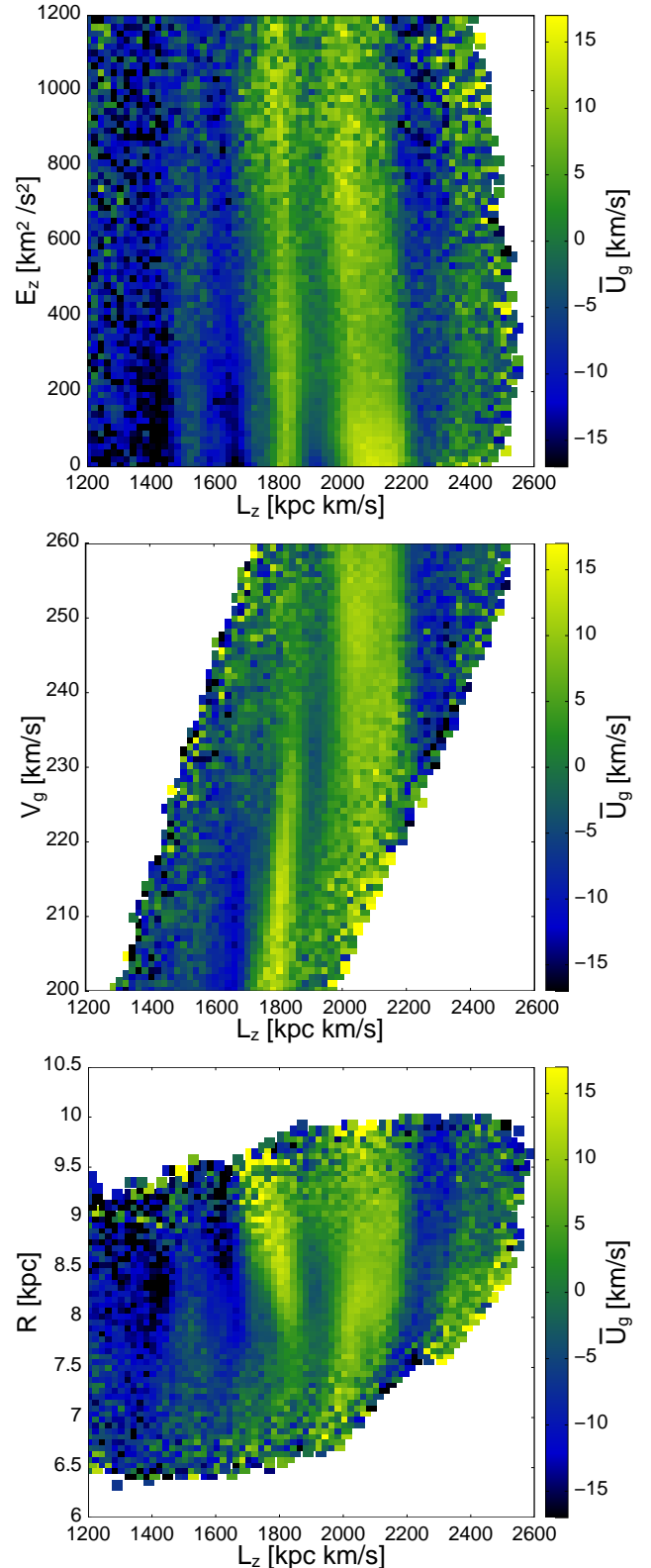


Figure 3. Mean radial velocity \bar{U}_g marked by colour on the L_z - E_z plane (top panel), the L_z - V_g plane (middle) and L_z - R (bottom). For each data bin we required a minimum star number of 10.

points are formally independent. However, in particular outside the core region in L_z , distance uncertainties will blur stars modestly along the x -axis. The magnitude selection in this sample strongly favours nearby stars, where Gaia parallaxes are very precise. The relative distance uncertainty distribution is provided in Fig. A2 of the Appendix, and peaks strongly around 2%. Systematic uncertainties will be of order 1% in the near field and slightly larger for remote stars.

It is instantly evident from Fig. 2 that \overline{U}_g varies with a wave-like pattern of a wavelength of about $300 \text{ kpc km s}^{-1}$, and an amplitude of order 4 km s^{-1} in \overline{U}_g . The pattern lies on top of larger scale fluctuations that are of order 10 km s^{-1} , i.e. we see that stars with low angular momentum have a net outwards motion relative to the LSR. The general trend of \overline{U}_g with R_g and hence L_z has been expected from prior models analysing the effects of the bar: Resonances of the bar are not only identified with features like the Hercules-stream (Dehnen 2000; Pérez-Villegas et al. 2017; Monari et al. 2018) (which itself has a strong average radial motion outwards), but the bar is also expected to cause a significantly non-zero \overline{U}_g all around the disc on its main resonances (Mühlbauer & Dehnen 2003), most notably the change of sign from negative to positive \overline{U}_g shortly outside the outer Lindblad-resonance due to the quadrupole moment of the bar. Similarly, we expect some imprints of the spiral arms both in \overline{U}_g vs. L_z and in \overline{U}_g vs. R . However, the wave-like nature of the pattern in \overline{U}_g is unexpected, and somewhat surprising. We can make out in total 4 peaks in \overline{U}_g , where the peak near the solar value of L_z 2070 kpc is wider and has a different appearance. We also experimented with different sample sizes, but it appears impossible at current stage to resolve more extreme values of L_z .

The first two questions to ask are of course: How confined is this feature to the plane, and, given that we detect it in L_z only, how confined is it in Galactocentric radius? This is answered in Fig. 3. To create the top panel, we introduced the local vertical energy relative to a star moving with no vertical velocity in the mid-plane:

$$E_z = \frac{1}{2}W^2 + \Phi(R, z) - \Phi(R, 0), \quad (1)$$

where $\Phi(R, z)$ is the galactic potential according to the mass model of McMillan (2017) at the position of the star, $\Phi(R, 0)$ is the potential at its projected position in the plane, and W^2 is the square of its vertical velocity component. Of course the vertical action would be a better conserved quantity, but E_z provides a straight-forward ordering in vertical extent along each orbit. We can see that the pattern persists with little change towards larger E_z , even though the maximum vertical energy plotted here corresponds to a vertical velocity of $W \sim 49 \text{ km s}^{-1}$ or respectively orbits extending to z 1 kpc altitude. In light of this stability, we expect the same result in vertical action. Curiously, the pattern slightly shifts in L_z with E_z : most prominently, the large peak around $L_z \sim 2100 \text{ kpc km s}^{-1}$ shifts to of order 80 kpc km s^{-1} lower L_z for large E_z values. Similar trends can be guessed for most of the remaining pattern, though the highest L_z feature hints at a slight rightward drift relative to the rest of the pattern, with the minimum of \overline{U}_g around $L_z \sim 2250 \text{ kpc km s}^{-1}$ deepening somewhat towards larger E_z . The left-ward drift can be expected if the peaks are physically connected to orbital

resonances, since the orbital frequencies should show a slight drift downwards for vertically more extended orbits.

The middle and bottom panels of Fig. 3 show the sample in the L_z - V_g and L_z - R planes. Of course, both plots are closely related by $L_z = RV_g$. Lines of constant radius in the middle panel run from lower-left to upper-right. The strong selection bias of the sample towards the Solar Galactocentric radius implies that we have a dearth of stars in the top left and bottom right corners of this plot. There is some dependence of the pattern on V_g . The most likely interpretation is that the wave-pattern has some dependence on the orbital phase, although at current stage it is difficult to disentangle this completely from sample selection effects. The sample selection shows more strongly in L_z vs R (bottom panel). Again there is a dependence on R , mostly in amplitude, but also with a surprising curving of the pattern at $R \sim 7.5 \text{ kpc}$. A part of the amplitude dependence can be ascribed to the asymmetry in distance biases.

To get a better grip on the R dependence and other parameters, we repeat the plot of Fig. 2 in Fig. 4 when selecting different ranges in each parameter. The top left panel of Fig. 4 shows \overline{U}_g vs. L_z for different bands of R . It is clear that for large R we have to lose all signal at low angular momenta, and for small R we have virtually no stars with large angular momentum. As indicated in the previous paragraph, for small $R < 7.5 \text{ kpc}$, the wave-pattern appears to get consistently weaker, especially in the low L_z range. However, this range is plagued by the larger uncertainties for remote stars, which blur out the peaks in \overline{U}_g .

This effect is also asymmetric in R and in L_z , which we make clear with an example: at large distances of order 2 kpc, a realistic Gaia parallax error of $\sigma_p \sim 0.05 \text{ mas}$ results in a distance uncertainty of $\sim 10\%$. In direction towards the Galactic Centre, a distance error affects the L_z measurement twice in the same direction: a star with $(R, V_g) = (6 \text{ kpc}, 200 \text{ km s}^{-1})$ will, if we underestimate its distance by 10%, be measured at $(R', V'_g) \sim (6.23 \text{ kpc}, 205 \text{ km s}^{-1})$, or respectively will have moved about a quarter wave-length of the wave-pattern in L_z . If we measure a star with high $V_g > 250 \text{ km s}^{-1}$ in the same place, the V_g velocity error will change sign and counteract the error in R . Analogously, errors for stars observed at large radii (towards the Galactic anticentre) with low V_g tend to cancel, while they will be additive for stars with large $V_g > V_{g\odot}$. This explains the main trends in \overline{V}_g and R . We have formally good data for low L_z and low V_g , but in particular at small R , the additive error budget will smear out the pattern in L_z . Similarly, the wave-pattern disappears at large R and small R , explaining the loss of signal at extreme values. In short, while our datasets have been optimised for unbiased distances, we still face a loss of signal to random errors.

The bottom left panel of Fig. 4 shows the wave-like pattern sliced in different bins of z . Focusing e.g. on the two most extreme altitude bands at $0.6 < |z|/\text{kpc} < 1$ vs. the rest of the sample, we can see that the pattern shifts symmetrically with increasing altitude. Note that the Galactic latitude cut of $b > 10^\circ$ implies that for small $|z|$ our sample is restricted to near solar radius stars. However, the quality difference with random errors to first order only affects the measured amplitude, so the consistent pattern/phase shift with $|z|$ is real. Further, the symmetry in z of the shift argues against systematic distance errors. The left-shift of the pat-

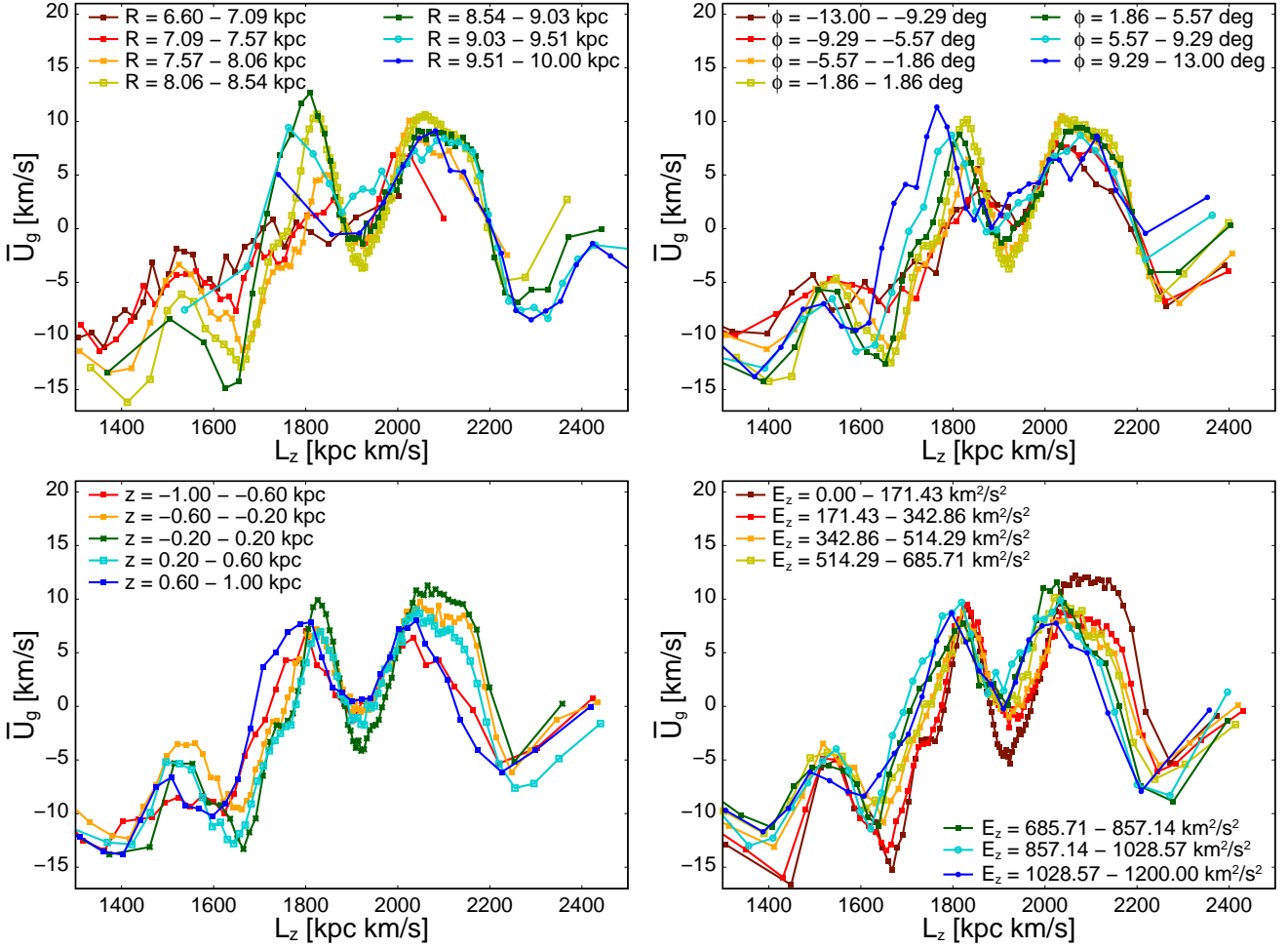


Figure 4. We use the same data as in Fig. 2, but divide the sample into equal width regions in Galactocentric radius R (top left panel), Galactic azimuth ϕ (top right), vertical altitude z (bottom left), and vertical energy E_z (bottom right).

tern can quite straight-forwardly be attributed to the slower orbital frequencies for stars reaching high altitude.

The phase shift with $|z|$ is consistent with the bottom right panel in Fig. 4, where we separate the sample in the vertical energy E_z of the stars. Again, with increasing vertical extent of the orbits, the pattern exhibits a constant shift to lower angular momentum. The shift is clearly detectable through the entire L_z range. We find again that with increasing E_z the signal tends to get weaker. Yet, again at least some of this loss of amplitude will be caused by the increasing distance uncertainties.

The top right panel tries to resolve the ϕ dependence of the wave-like structure. This is particular interesting, since it can give us clues about the perturbation causing the pattern and the wavenumber of this perturbation. The phase shift with ϕ is already visible to the naked eye. In particular, the left prominent peak shifts systematically to the left with increasing ϕ , i.e. resembles a trailing pattern. Again, measurements at large $|\phi|$ are ridden with distance uncertainties, since all their stars are at the fringes of our quality limits, but this is a promising start for a further investigation. Unlike $|z|$, where all peaks shifted consistently, the behaviour in ϕ indicates that this is a superposition of at least two causes/modes with different wavenumber.

4.2 Constraining the phase shift

Just having seen the phase shift of the pattern with Galactic azimuth ϕ , we attempt to quantify it and to derive the wavenumber m . Any fit will be far from perfect, since the changing distance error distribution will increasingly wash out the wave pattern towards larger $|\phi|$. The idea is that if we find a half-way decent fit function for a local, well-constrained part of the sample that also gives reasonable fits for the adjacent regions, the alignment of data and the fit should be enough to pick out the average amount of phase shift, even with imperfect parameters for amplitude and wavelength in L_z . If we then assume that we have made a reasonable choice for the wavelength of the fit function, we can estimate the wavenumber m from the slope of the fit in δL_z vs. ϕ by dividing it by the wavelength.

To find the best-guess fit function, we picked a subsample restricted to 8.06–8.55 kpc in Galactocentric radius and -1.86 to 1.86° in azimuth, which is depicted in the top panel of Fig. 5. As can be seen from the blue line in the plot, the pattern is well-fit by a superposition of a fast and a slow wave:

$$\overline{U}_g(L_z) = \sum_{i=1}^2 A_i \sin \left((L_z + \delta_{L_z,i}) \cdot \frac{2\pi}{\lambda_i} \right) + t. \quad (2)$$

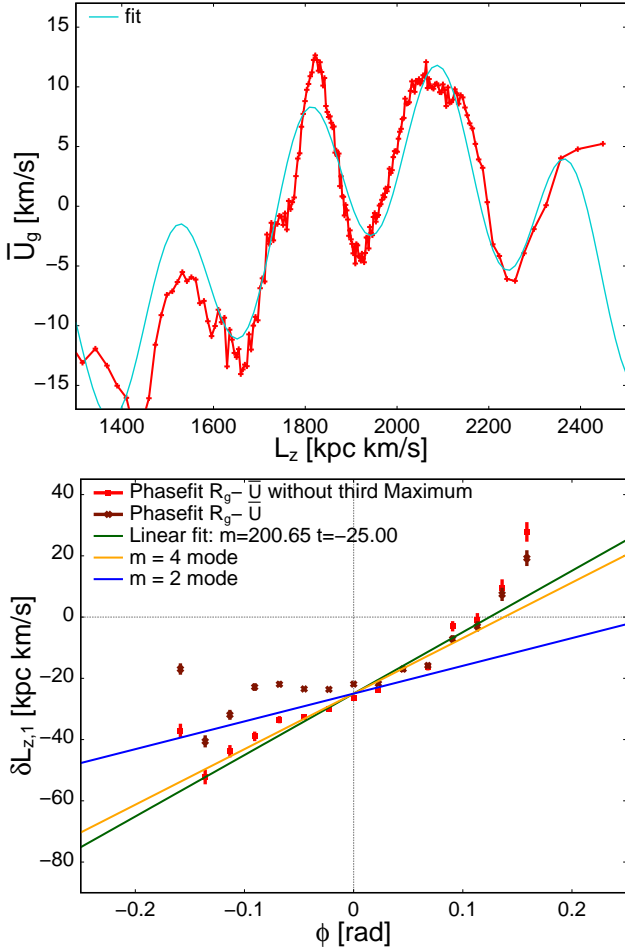


Figure 5. Top panel: Fit of function 2 to a data sample restricted to a box of radial width of 0.49 kpc and angular width of 3.7° centred around the sun. Bottom panel: The phase shift δ_1 via eq. 2 with increasing azimuth. We compare two fits, one for a sample including the whole L_z range and one fit where we exclude the angular momentum region of the third peak between $1950 \text{ kpc km s}^{-1}$ and $2250 \text{ kpc km s}^{-1}$.

We held constant our amplitudes $A_1 = 7.0 \text{ km s}^{-1}$, $A_2 = 8.0 \text{ km s}^{-1}$ and wavelengths $\lambda_1 = 285 \text{ kpc km s}^{-1}$, $\lambda_2 = 1350 \text{ kpc km s}^{-1}$, $\delta L_{z,2} = 1010$ and $t = -2.877 \text{ km s}^{-1}$ and varied the phase $\delta L_{z,1}$ for azimuthal slices of width 1.68° , fitting to the full sample in each range of ϕ .

The lower panel of Fig. 5 shows the fitted $\delta L_{z,1}$ over the average azimuth in their bin and assumed a linear fit to derive the average phase shift in $\text{kpc km s}^{-1} \text{ rad}^{-1}$ as slope of that fit. We found that taking the whole sample into account resulted in a slope of $(97 \pm 32) \text{ kpc km s}^{-1} \text{ rad}^{-1}$.

To help a further analysis of the phase shift, Fig. 6 shows the complete azimuthal plane of our sample. It is clear that the two prominent maxima behave differently with the left one shifting more rapidly to large L_z for small azimuth. This is also the main problem when fitting, as the maxima nearly coincide at small ϕ . Together with the increased distance uncertainties, fits at large $|\phi|$ become unreliable. The peak near $L_z \sim 2100 \text{ kpc km s}^{-1}$ shows again a clearly different behaviour from the rest of the pattern, with a significantly lower phase shift in ϕ . We therefore re-fitted eq. 2,

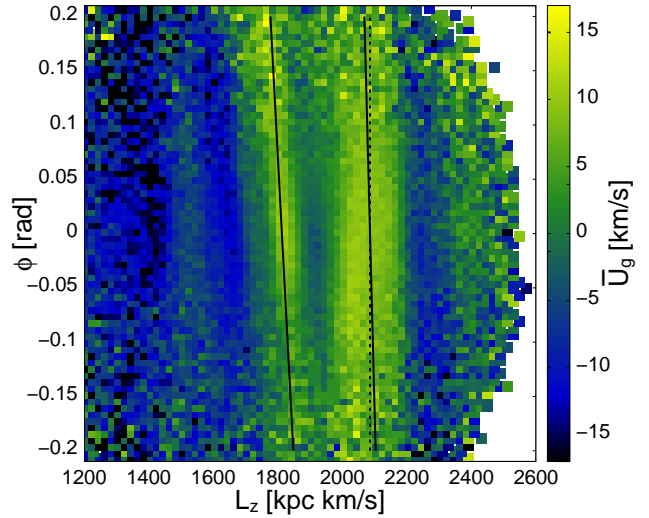


Figure 6. The mean U_g velocity component in bins of ϕ and L_z . We can see the systematic phase-shift of the single peaks and troughs. It becomes quite clear that the most prominent peak appears to have a lower wavenumber m than the rest of the pattern. To guide the eye, we have entered lines for phase shifts in L_z with $m = 4$ to the peak at $L_z(\phi = 0) = 1820$ and $m = 2$ as well as a vertical dashed line for the wide peak at $L_z(\phi = 0) = 2100 \text{ kpc km s}^{-1}$.

while excluding stars with $1950 < L_z / (\text{kpc km s}^{-1}) < 2250$. The resulting phase shifts are shown with bright red error bars in the bottom panel of Fig. 5). The best-fit linear slope for these (shown with the green line) is $dL_z/d\phi = (202 \pm 22) \text{ kpc km s}^{-1} \text{ rad}^{-1}$. Again, the different results for the phase shift after excluding the broad peak in \overline{U}_g from the sample indicates that two causes with different wavenumbers are responsible for the pattern. If we believe the wavelength of the fit function, the phase shift translates to a wavenumber $m = 4.4 \pm 0.5$, suggesting an $m = 4$ perturbation.

We tried to make this more evident by introducing lines in Fig. 6 depicting different linear phase shifts $dL_z/d\phi$ at the positions of the maxima. We can see that indeed the maximum near $L_z \sim 1850 \text{ kpc km s}^{-1}$ is well approximated by a phase shift of $180 \text{ kpc km s}^{-1} \text{ rad}^{-1}$ (consistent with a $m = 4$ -mode). The broad peak around $L_z \sim 2100 \text{ kpc km s}^{-1}$ is too wide to allow for a firm statement. It is incompatible with the large $dL_z/d\phi$, but consistent with any scenario between a moderate $dL_z/d\phi = 90 \text{ kpc km s}^{-1} \text{ rad}^{-1}$ (solid line, consistent with a $m = 2$ -mode) or even a constant phase (dashed line).

We conclude that the observed pattern is consistent with a superposition of two trailing patterns in Galactic azimuth.

4.3 Connecting to the vertical wave pattern

In Fig. 7 we show the \overline{U}_g - L_z pattern overlayed with the same evaluation for \overline{W} vs. L_z . We instantly see that the vertical wave-pattern detected by Schönrich & Dehnen (2018) appears to be strongly correlated with the \overline{U}_g wave discussed in this paper: the wave-peaks in \overline{W} appear to line up with the outer troughs of the \overline{U}_g wave. This could be a mere coincidence, but the degree of alignment suggests rather a

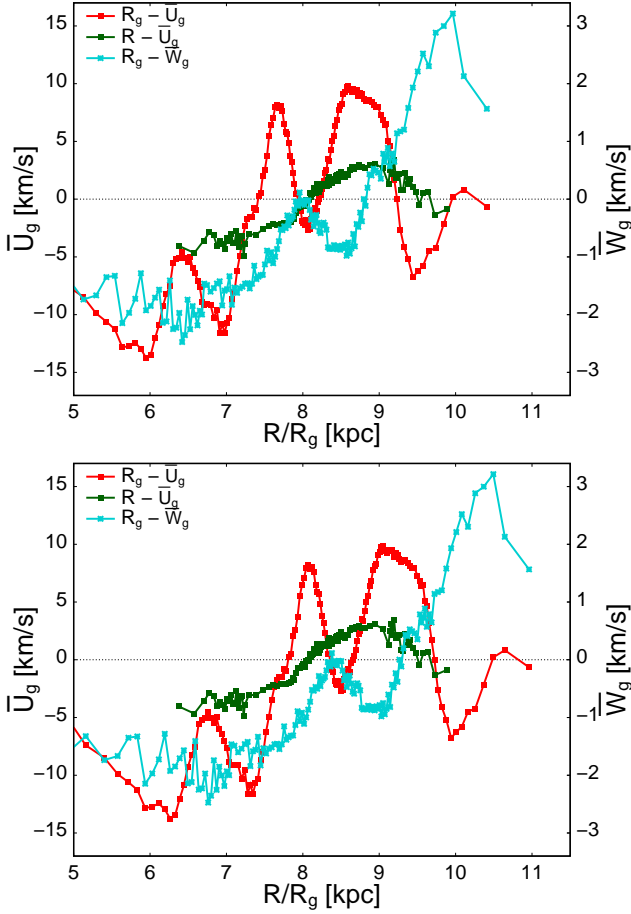


Figure 7. Comparison of the signal in $R - \overline{U}_g$ and the one in $R_g - \overline{U}_g$ and $R_g - \overline{W}$. To highlight the alignments of the extrema and make the weaker $R_g - \overline{W}$ signal better visible we stretched this graph by a factor of five. The two panels use the same data, but the lower one accounts for asymmetric drift effects in the derivation of L_z by taking $R_g = L_z / \overline{V}_g = L_z / (226 \text{ km s}^{-1})$ instead of $R_g = L_z / V_{c,\odot} = L_z / (238 \text{ km s}^{-1})$.

physical correlation. As the amplitude in \overline{W} is a factor ~ 5 , our sample could not yield a reliable signal for \overline{W} vs. ϕ to track the phase shift.

Many hypotheses can be drawn for this alignment. Of course a common origin could be suggested if both the radial and the vertical wave originate from the same dwarf galaxy impact (e.g. Binney & Schönrich 2018). This has not been predicted, but it would not be a surprise, since the phase space spiral is predicted and measured both in \overline{W} and \overline{U}_g . Alternatively, a bar buckling would cause both a radial and a vertical perturbation at the same time (Khoperskov, Sergey et al. 2019), but again it is not evident, why this pattern would lead to a seemingly matching wavelength in L_z . Again, we could not find any prediction of any such signal in the literature, apart from Masset & Tagger (1997). In their paper, the authors predict that near an outer Lindblad resonance a spiral wave should interact with the galactic warp to produce a coupled horizontal and vertical wave. However, this effect should be antisymmetric around the Galactic plane.

We thus examine the signals separated by galactic hemi-

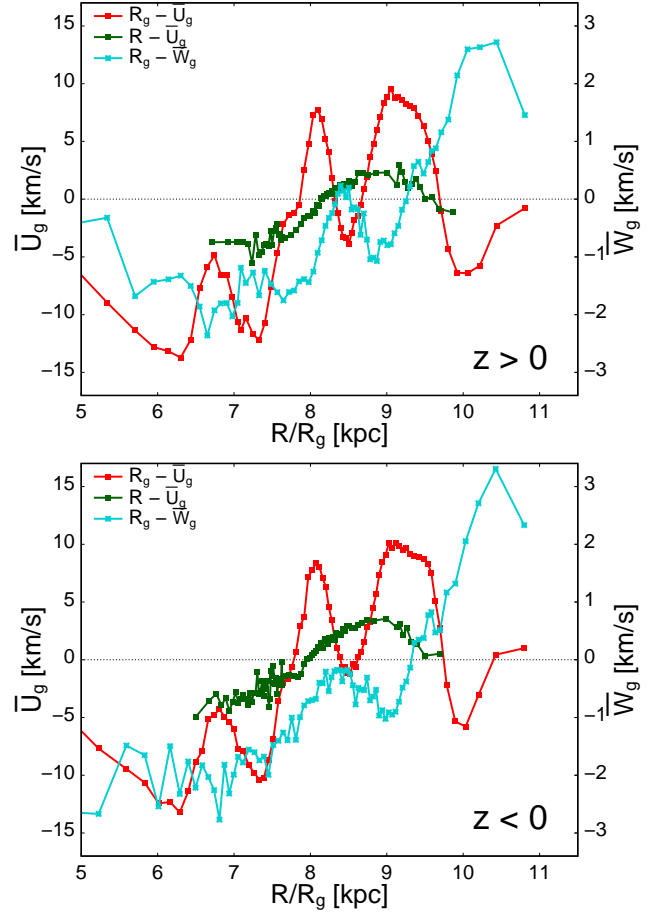


Figure 8. Same plot as in the lower panel of Fig. 7, but for positive z (upper panel) and negative z (lower panel).

sphere in Fig. 8. We find a mild difference of the vertical and radial velocity patterns above and below the Galactic plane, with a mildly stronger overlap of the extrema in \overline{U}_g and \overline{W} for positive z . While \overline{U}_g is slightly decreased in the Northern hemisphere (both when taken with respect to R and to L_z), \overline{W} is shifted upwards in our plot and shows a borderline significant third peak near $R_g \sim 7.2 \text{ kpc}$. The general alignment is however clearly visible for both hemispheres.

Fig. 7 and Fig. 8 also compare the \overline{U}_g vs. R pattern to the \overline{U}_g - L_z dependence. Trends of \overline{U}_g with R have been predicted at least since the time of Hipparcos (Mühlbauer & Dehnen 2003). Later, hints for a gradient in \overline{U}_g vs. R have been found e.g. by Siebert et al. (2012) in RAVE data. They were explained by Faure et al. (2014), who showed with a 3D test-particle simulation that a spiral structure can be responsible for the observed pattern. Liu et al. (2018) continued along the line of argumentation by Mühlbauer & Dehnen (2003) and suggested that a bar is responsible for the dependence of \overline{U}_g on R . The simple pattern that we find in \overline{U}_g vs. R very strongly resembles and qualitatively agrees with this prediction from Mühlbauer & Dehnen (2003). We also note that the \overline{U}_g vs. R dependence in Fig. 7 resembles the findings in fig. 12 of Gaia Collaboration et al. (2018b). It is also evident that this dependence is mostly a washed-out (by epicyclic motions of

the orbits around their guiding centre) version of what we see in L_z . To make this clearer, we repeat the plot of the top panel of Fig. 7 in the bottom panel, with one change: instead of using the assumed circular velocity $V_c = 238 \text{ km s}^{-1}$ to translate L_z to R_g , we add an asymmetric drift and use $\overline{V}_g = 226 \text{ km s}^{-1}$ to translate. Unsurprisingly, this results in a good agreement between the patterns in L_z and R .

5 CONCLUSION

We have for the first time found a prominent wave-like pattern in mean radial velocities \overline{U}_g vs. angular momentum L_z in the RV subsample of Gaia DR2. The amplitude of the pattern is of order 4 km s^{-1} with a wavelength of about $285 \text{ km s}^{-1} \text{ kpc}$ in L_z or $\sim 1.2 \text{ kpc}$ in guiding centre radius R_g . To our knowledge, this pattern has not been directly predicted by any Galaxy model, though of course the offsets in \overline{U}_g predicted in the V_g - \overline{U}_g plane by papers like Monari et al. (2018) for distinct entities like the Herkules stream should be related to our finding.

The structure is evidently not bound to a single Galactocentric radius R . We can detect it in a region of $\sim 7 - 10 \text{ kpc}$, i.e. a band of $\sim 3 \text{ kpc}$ around the Sun. There is a slight drift of the ridges towards smaller L_z for small V_g , however the dependence of L_z on V_g and R makes it hard to raise definite claims for the evolution of the pattern with these quantities.

The wave-like structure is not limited to kinematically cold thin-disc stars. We binned the sample in the local vertical energy E_z and found that the wave-like pattern persists to stars with $E_z \sim 1200 (\text{km s}^{-1})^2$, i.e. stars with orbits passing beyond thick disc altitudes $|z| > 1 \text{ kpc}$. For these kinematically very hot populations, the amplitude appears to be roughly half of the amplitude for kinematically cold stars, but this decrease is likely over-estimated due to larger distance uncertainties blurring the pattern. Towards larger E_z the pattern shifts to the left, i.e. smaller L_z with a trend of about $0.05 \text{ kpc km s}^{-1} / (\text{km s}^{-1})^2$. This is likely connected to the slower radial frequencies of stars at higher altitudes.

Most interestingly, the Gaia dataset is sufficiently extended that we can detect the slope of the ridges against the Galactic angle ϕ . Without specifying a model, we can thus draw conclusions on the physical cause of the pattern: All ridges tend towards lower L_z for larger ϕ , consistent with a trailing pattern in Galactic azimuth. However, there is a clear deviation with the peak in positive U_g near $L_z \sim 2100 \text{ km s}^{-1} \text{ kpc}$ showing only about half the change of the rest of the pattern. If we filter out this peak from our analysis, the slope of the remaining pattern in L_z vs. ϕ is consistent with an $m = 4$ wave-number, while the broad $L_z \sim 2100 \text{ kpc km s}^{-1}$ peak has a drift consistent with an $m = 2$ mode. Hence, it is logical to associate the broad peak with an $m = 2$ excitation, and most likely the outer Lindblad resonance of the Galactic bar, while the majority of the remaining pattern is consistent with an $m = 4$ excitation. A likely cause is the spiral pattern of the Milky Way. Another possible reason are higher order ($m \geq 4$) contributions to the bar potential.

Comparing the \overline{U}_g vs. R_g pattern to the similar pattern in \overline{U}_g vs. R , we find that the overall peak in \overline{U}_g vs. R (which is already present in the analysis of Gaia Collaboration et al.

(2018b)) around $R \sim 8.8 \text{ kpc}$ is in line with the \overline{U}_g vs. R_g pattern being smeared out by epicyclic motions, once we account for the fact that the latter is shifted towards slightly larger values of R_g by the asymmetric drift.

Last, we compared the newly found U_g vs. L_z pattern to the wave-like structure found by Schönrich & Dehnen (2018) in DR1. This pattern is still present in Gaia DR2, but its wavelength in L_z is longer than the wavelength of the radial velocity pattern. The two peaks in W vs. L_z clearly visible in this selection fall roughly in the region of two troughs of L_z . There is a hint of a third peak in \overline{W} coinciding with the lowest \overline{U}_g trough in L_z , particularly visible in the northern galactic hemisphere.

6 ACKNOWLEDGEMENTS

It is a pleasure to thank J. Binney, W. Dehnen, and R. Chiba for helpful comments. JF thanks the Stiftung Maximilianum, the Ev. Studienwerk Villigst and the Max-Weber-Programm for their support and Merton College Oxford for their hospitality, without which this work would never have been undertaken. RS is supported by a Royal Society University Research Fellowship. This work was performed using the Cambridge Service for Data Driven Discovery (CSD3), part of which is operated by the University of Cambridge Research Computing on behalf of the STFC DiRAC HPC Facility (www.dirac.ac.uk). The DiRAC component of CSD3 was funded by BEIS capital funding via STFC capital grants ST/P002307/1 and ST/R002452/1 and STFC operations grant ST/R00689X/1. DiRAC is part of the National e-Infrastructure. This work has made use of data from the European Space Agency (ESA) mission *Gaia* (<https://www.cosmos.esa.int/gaia>), processed by the *Gaia* Data Processing and Analysis Consortium (DPAC, <https://www.cosmos.esa.int/web/gaia/dpac/consortium>). Funding for the DPAC has been provided by national institutions, in particular the institutions participating in the *Gaia* Multilateral Agreement.

REFERENCES

- Antoja T., et al., 2018, *Nature*, 561, 360
- Arenou F., et al., 2018, *A&A*, 616, A17
- Bergemann M., et al., 2018, *Nature*, 555, 334
- Binney J., Schönrich R., 2018, *MNRAS*, 481, 1501
- Cropper M., et al., 2018, *A&A*, 616, A5
- D’Onghia E., Madau P., Vera-Ciro C., Quillen A., Hernquist L., 2016, *ApJ*, 823, 4
- Dehnen W., 1998, *AJ*, 115, 2384
- Dehnen W., 2000, *AJ*, 119, 800
- Drimmel R., Spergel D. N., 2001, *ApJ*, 556, 181
- Drimmel R., Smart R. L., Lattanzi M. G., 2000, *A&A*, 354, 67
- Faure C., Siebert A., Famaey B., 2014, *MNRAS*, 440, 2564
- Gaia Collaboration et al., 2016a, *A&A*, 595, A1
- Gaia Collaboration et al., 2016b, *A&A*, 595, A1
- Gaia Collaboration et al., 2018a, *A&A*, 616, A1
- Gaia Collaboration et al., 2018b, *A&A*, 616, A11
- Gillessen S., Eisenhauer F., Trippe S., Alexander T., Genzel R., Martins F., Ott T., 2009, *ApJ*, 692, 1075
- Khoperskov, Sergey Di Matteo, Paola Gerhard, Ortwin Katz, David Haywood, Misha Combes, Françoise Berczik, Peter Gomez, Ana 2019, *A&A*, 622, L6

- Khoperskov S., Di Matteo P., Gerhard O., Katz D., Haywood M., Combes F., Berczik P., Gomez A., 2018, arXiv e-prints,
- Laporte C. F. P., Johnston K. V., Gómez F. A., Garavito-Camargo N., Besla G., 2018, *MNRAS*, **481**, 286
- Lindgren L., et al., 2018, *A&A*, **616**, A2
- Liu C., Xu Y., Wang H., Wan J., 2018, in Chiappini C., Minchev I., Starkenburg E., Valentini M., eds, IAU Symposium Vol. 334, Rediscovering Our Galaxy. pp 109–115 (arXiv:1712.03977), doi:10.1017/S1743921317010870
- Masset F., Tagger M., 1997, *A&A*, **318**, 747
- McMillan P. J., 2017, *MNRAS*, **465**, 76
- Monari G., Famaey B., Siebert A., Wegg C., Gerhard O., 2018, arXiv e-prints,
- Mühlbauer G., Dehnen W., 2003, *A&A*, **401**, 975
- Pérez-Villegas A., Portail M., Wegg C., Gerhard O., 2017, *ApJ*, **840**, L2
- Perryman M. A. C., et al., 1997, *A&A*, **323**, L49
- Poggio E., et al., 2018, *MNRAS*, **481**, L21
- Reylé, C. Marshall, D. J. Robin, A. C. Schultheis, M. 2009, *A&A*, **495**, 819
- Sartoretti P., et al., 2018, *A&A*, **616**, A6
- Schönrich R., 2012, *MNRAS*, **427**, 274
- Schönrich R., Aumer M., 2017, *MNRAS*, **472**, 3979
- Schönrich R., Dehnen W., 2018, *MNRAS*, **478**, 3809
- Schönrich R., Binney J., Dehnen W., 2010, *MNRAS*, **403**, 1829
- Schönrich R., Binney J., Asplund M., 2012, *MNRAS*, **420**, 1281
- Schönrich R., McMillan P., Eyer L., 2019, arXiv e-prints,
- Seabroke G., Ciucă I., Cropper M., Kawata D., Baba J., Grand R. J. J., Hunt J. A. S., 2018, *MNRAS: Letter*, **479**, L108
- Siebert A., et al., 2012, *MNRAS*, **425**, 2335
- Stassun K. G., Torres G., 2018, preprint, (arXiv:1805.03526)
- Weinberg M. D., 1995, *ApJ*, **455**, L31
- Xu Y., Newberg H. J., Carlin J. L., Liu C., Deng L., Li J., Schönrich R., Yanny B., 2015, *ApJ*, **801**, 105
- Zinn J. C., Pinsonneault M. H., Huber D., Stello D., 2018, preprint, (arXiv:1805.02650)

APPENDIX A: SAMPLE SELECTION AND QUALITY CUTS

We dedicate this Appendix to some further quality tests in order to ascertain the significance of our findings and test for possible systematic effects. First, we want to make sure that the found pattern in $L_z - \bar{U}_g$ is not dependent on the choice of assumptions on parallax error $\delta\sigma_p$ and parallax bias δp in Gaia DR2. In the main text, we used exclusively the sample with $\delta\sigma_p = 0.043$ mas and $\delta p = 0.054$ mas. Fig. A1 demonstrates that choosing any sample has only marginal consequences for the derived pattern of \bar{U}_g vs. L_z , with a minor deviation for very small L_z in the third sample, which uses $\delta\sigma_p = 0$ and $\delta p = 0.048$ mas. This is easily understood, since the lack of an additional error term in σ_p allows for a further extent of the sample under our quality cut $p/\sigma_p > 10$. We also note that this sample has to be treated with caution, since there is good evidence that the Gaia pipeline values for σ_p are underestimated.

Fig. A2 shows the distribution of the standard deviation of the distances to estimated distance ratio, to help the reader assess the impact of distance uncertainties on our results. The relative error σ_s/\bar{s} of the expected distance \bar{s} peaks at around 2%. The quality cut $p/\sigma_p > 10$ of course results in a similar cutoff in σ_s/\bar{s} , removing basically all stars with an estimated relative distance uncertainty greater than $\sim 11\%$. The strong peak at small relative errors results from

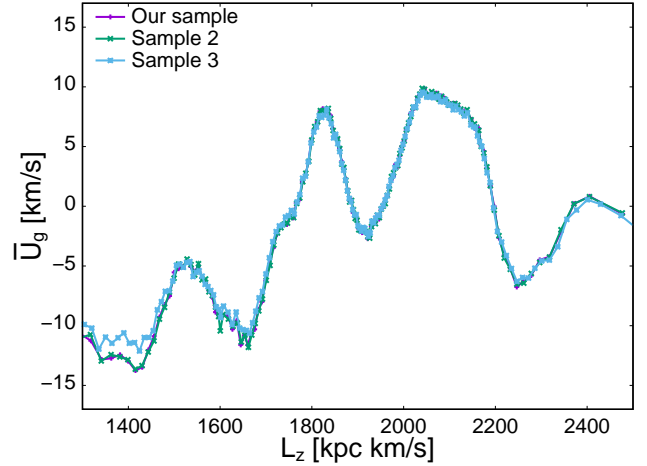


Figure A1. Comparison of the $L_z - U_g$ pattern for three data samples derived from Gaia data. Sample 2 also increases the parallax error $\sigma_p = \sqrt{\sigma_p'^2 + (\delta\sigma_p)^2}$ by $\delta\sigma_p = 0.043$ mas but corrects for an parallax offset $\delta p = 0.048$ mas and no increase of the parallax error, i.e. $\delta\sigma_p = 0$. It is the most extended, but also the one with the largest relative uncertainties (the formal error uncertainty in that sample is up to a factor 2 smaller for most stars), so the signal in L_z will be a little more blurred. Further information on the derivation of our samples can be found in Schönrich et al. (2019)

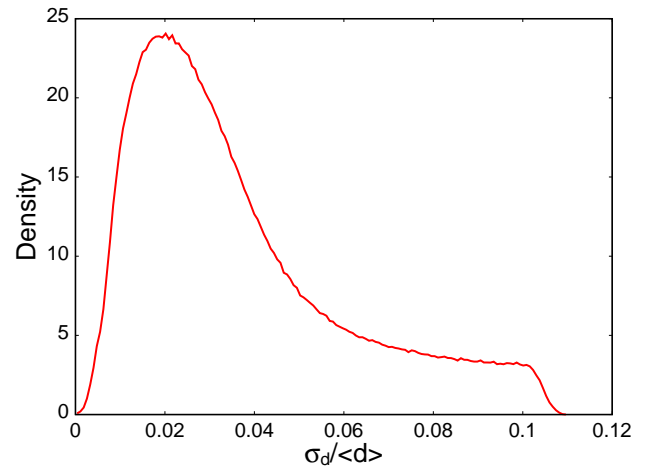


Figure A2. Distribution of distance standard deviation over estimated distance for our sample after applying the quality cuts

the magnitude based selection in the Gaia RV subset, which strongly favours nearby stars. Note that the large distance uncertainties are of course found predominantly near the distant rim of our sample, the consequence of which we will examine further below.

It is important to consider how different demands on the quality of our sample affect the pattern. Throughout this work, we required (in addition to the quality cuts suggested in section 8 of Schönrich et al. (2019)) a quality cut $p/\sigma_p > 10$. However, as Fig. A3 shows, different p/σ_p ratios have only very little influence on the strength of the pattern, with a slightly lower amplitude for lower quality requirements due to random errors.

As our discussed wave pattern proved especially hard

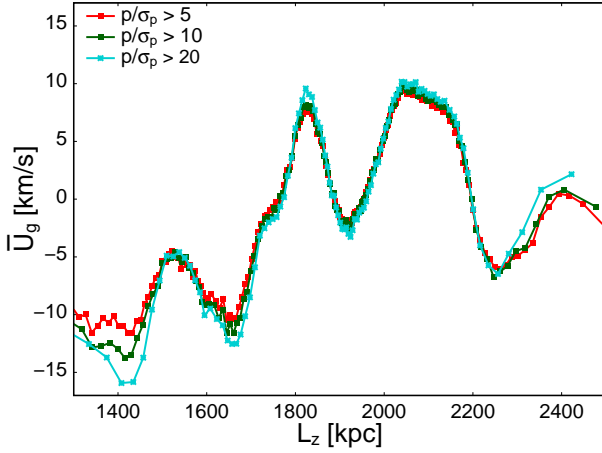


Figure A3. Comparison of the $L_z - \overline{U}_g$ pattern for different quality cuts in parallax over parallaxerror.

to resolve in radius, we repeat the plot of the bottom panel of Fig. 3 in the upper panel of Fig. A4 with a parallax cut of $p/\sigma_p > 20$. We find that the radial data range is strongly affected by this requirement and that the peculiar bent in \overline{U}_g for radii of 7.5 kpc cannot be resolved anymore. It is thus likely that a definitive analysis of this has to await Gaia DR3.

As discussed in section 4.1, any pattern in the angular momentum should be increasingly washed out with increasing L_z uncertainty and should nearly disappear for an uncertainty exceeding roughly half a wavelength of the pattern. Stars at small R are particularly prone due to the additive effect of a distance error both on R and V_g in this region. We tried to estimate the error in L_z from the distance uncertainty by taking $\sigma_{L_z} \approx \sigma_s \cdot dL_z/ds$, where s is the expected distance to the star and σ_s the standard deviation of the distance probability distribution. The resulting pattern of the averaged σ_{L_z} (in quadrature) in the L_z – R plane can be found in the lower panel of Fig. A4. Consistent with our findings in the main text, in the red regions of this figure we do not expect to still find a clear \overline{U}_g -signal, as a $\sigma_{L_z} > 70 \text{ kpc km s}^{-1}$ exceeds one quarter of the wave-length of the observed pattern.

This paper has been typeset from a \LaTeX file prepared by the author.

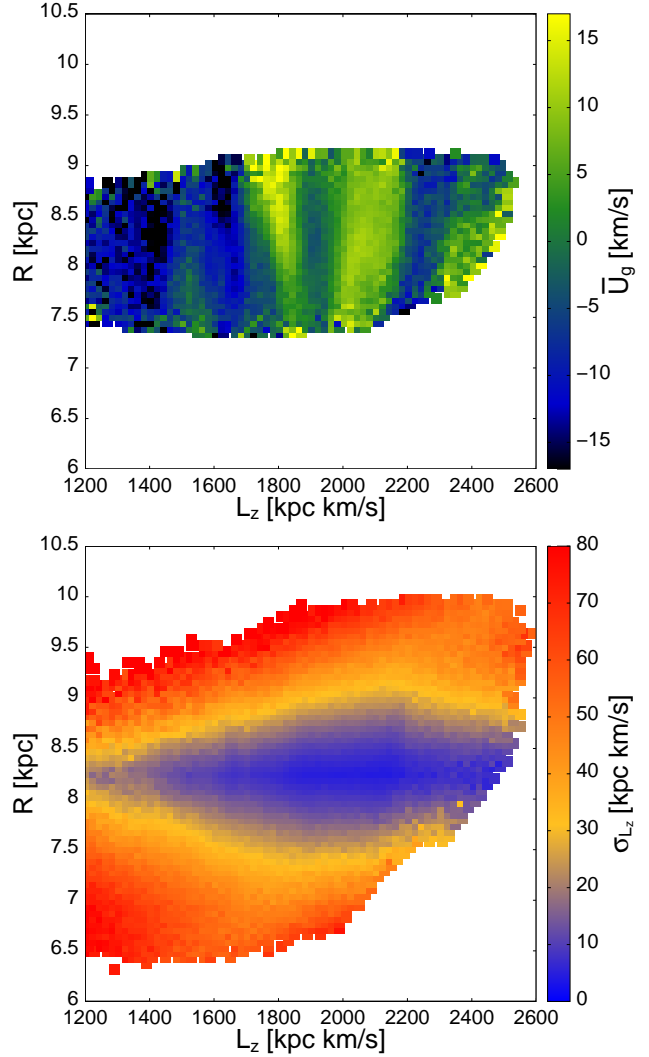


Figure A4. Upper Panel: Same Plot as in the lower panel of Fig. 3 but with the higher quality requirement of parallax over parallax error bigger 20. Lower panel: Estimated standard deviation of the angular momentum L_z from the distance error.